



# Enhanced photocatalytic inactivation of *Escherichia coli* by a novel Z-scheme g-C<sub>3</sub>N<sub>4</sub>/m-Bi<sub>2</sub>O<sub>4</sub> hybrid photocatalyst under visible light: The role of reactive oxygen species

Dehua Xia<sup>a</sup>, Wanjun Wang<sup>b,\*</sup>, Ran Yin<sup>c</sup>, Zhifeng Jiang<sup>a,d</sup>, Taicheng An<sup>b</sup>, Guiying Li<sup>b</sup>, Huijun Zhao<sup>e,f</sup>, Po Keung Wong<sup>a,\*</sup>

<sup>a</sup> School of Life Sciences, The Chinese University of Hong Kong, Shatin, NT, Hong Kong SAR, China

<sup>b</sup> Institute of Environmental Health and Pollution Control, School of Environmental Science and Engineering, Guangdong University of Technology, Guangzhou 510006, Guangdong, China

<sup>c</sup> Department of Civil and Environmental Engineering, The Hong Kong University of Science and Technology, Clear Water Bay, Kowloon, Hong Kong SAR, China

<sup>d</sup> Institute for Energy Research, Jiangsu University, Zhenjiang, 212013, Jiangsu, China

<sup>e</sup> Centre for Clean Environment and Energy, Griffith Scholl of Environment, Griffith University, Queensland 4222, Australia

<sup>f</sup> Laboratory of Nanomaterials and Nanostructures, Institute of Solid State Physics, Chinese Academy of Sciences, Hefei 230031, Anhui, China

## ARTICLE INFO

### Article history:

Received 2 March 2017

Received in revised form 8 May 2017

Accepted 10 May 2017

Available online 11 May 2017

### Keyword:

*E. coli* inactivation

g-C<sub>3</sub>N<sub>4</sub>/m-Bi<sub>2</sub>O<sub>4</sub>

Charge transfer

Z-scheme

Bacterial destruction

## ABSTRACT

Biohazards are widely present in wastewater, and contaminated water can arouse various waterborne diseases. Therefore, effective removal of biohazards from water is a worldwide necessity. In this study, a novel all-solid-state Z-scheme g-C<sub>3</sub>N<sub>4</sub>/m-Bi<sub>2</sub>O<sub>4</sub> heterojunction was constructed using a facile hydrothermal approach. Using the optimum g-C<sub>3</sub>N<sub>4</sub>/m-Bi<sub>2</sub>O<sub>4</sub> (1:0.5), 6 log<sub>10</sub> cfu/mL of *E. coli* K-12 could be completely inactivated within 1.5 h under visible light irradiation, while only 1.2 log<sub>10</sub> cfu/mL and 3.2 log<sub>10</sub> of *E. coli* K-12 were inactivated by pure g-C<sub>3</sub>N<sub>4</sub> and Bi<sub>2</sub>O<sub>4</sub> under the same experimental conditions respectively. Emphasis was placed on identifying how the charge transfers across the g-C<sub>3</sub>N<sub>4</sub>/m-Bi<sub>2</sub>O<sub>4</sub> heterojunction and a Z-scheme charge transfer mechanism was verified by reactive species trapping and quantification experiments. The Z-scheme charge separation within g-C<sub>3</sub>N<sub>4</sub>/m-Bi<sub>2</sub>O<sub>4</sub> populated electrons and holes into the increased energy levels, thereby enabling one-step reduction of O<sub>2</sub> to H<sub>2</sub>O<sub>2</sub> and facilitating more generation of holes. This greatly accelerated photocatalytic efficiency on the inactivation of *E. coli*. Moreover, microscopy images indicate that cell structures were damaged and intracellular components were leaked out during the photocatalytic inactivation process. This study suggests that the newly fabricated Z-scheme g-C<sub>3</sub>N<sub>4</sub>/m-Bi<sub>2</sub>O<sub>4</sub> is a promising photocatalyst for water disinfection.

© 2017 Elsevier B.V. All rights reserved.

## 1. Introduction

With global climate changes and increasing populations, the shortages of fresh water require increased water recycling and reuse [1,2]. Biohazards, such as bacteria, viruses, and fungi are widely present in drinking water sources (e.g., surface water and groundwater) and pose significant health risks to human [3,4]. Unfortunately, conventional water disinfection methods, including UV irradiation or chemical disinfection using ozone and chlorine, all have some disadvantages [5–9]. For example, UV irradiation could

effectively inactivate biohazards, but the high energy consumption and operational cost limit their application [5,6]. Meanwhile, an increased dosage of chemical disinfectants is needed for the inactivation of persistent biohazards, and it will increase the formation of disinfection byproducts (DBPs) [7–9]. Moreover, a number of biohazards are naturally resistant to UV and chlorination [6]. Therefore, effectively removing biohazards from water is a challenge that has received sustained attention [10–12], and versatile new technologies are highly needed to efficiently inactivate biohazards without causing secondary pollution.

Semiconductor-based photocatalysis has been recognized as a promising technology to purify water and wastewater, including decomposing a wide array of organic contaminants, as well as inactivating pathogenic biohazards, attributed to its superior photocatalytic activity, nontoxic and stable properties [13–16].

\* Corresponding authors.

E-mail addresses: [wanjun.w@163.com](mailto:wanjun.w@163.com) (W. Wang), [pkwong@cuhk.edu.hk](mailto:pkwong@cuhk.edu.hk) (P.K. Wong).

Therefore, the search of suitable photocatalysts has been an intensively pursued topic. Over the last few decades, the development of visible-light-driven photocatalysts has evolved from modified TiO<sub>2</sub> to non-TiO<sub>2</sub> based semiconductor materials, such as metal oxides, sulfides, oxynitrides or oxysulfides and even non-metal based graphitic carbon nitride (g-C<sub>3</sub>N<sub>4</sub>) [17–20]. Among these compounds, the simple g-C<sub>3</sub>N<sub>4</sub> is much more promising for practical application, because it has unique advantages of simple structure, low costs, facile synthesis and easy to scale up for commercial applications [21]. Moreover, the delocalized conjugated p structures in g-C<sub>3</sub>N<sub>4</sub> have been found to lead to rapid photo-induced charge separation and a relatively slow charge recombination [22]. Furthermore, its relatively narrow band gap originating from the tri-s-triazine units connected with planar amino groups leads to efficient light harvesting within the visible light region and electric conductivity [23]. Previous work has demonstrated that g-C<sub>3</sub>N<sub>4</sub> could inactivate  $2 \times 10^6$  cfu/mL of *E. coli* within 4-h under visible light irradiation [24].

However, the photocatalytic disinfection activity of pristine g-C<sub>3</sub>N<sub>4</sub> is far from satisfactory with light response limited to 430 nm. To fully utilize the whole sunlight spectrum, it is important to extend the light response to longer wavelength regions. Heterojunctions formation is an effective strategy to simultaneously modulate the light absorption property and enhance the interfacial charge transportation efficiency [25,26]. For example, a heterojunction with a Z-scheme charge transfer process can efficiently separate the photogenerated electrons and holes into two photosystems through an electron mediator, helping spatially isolate the oxidation and reduction reaction sites and thus enhancing the photocatalytic activity [27,28]. Recently, a novel bismuth (Bi)-based simple oxide photocatalyst (i.e., monoclinic dibismuth tetraoxide, m-Bi<sub>2</sub>O<sub>4</sub>) was developed. With mixed valent states (Bi<sup>3+</sup> and Bi<sup>5+</sup>) and a narrow band gap of 2.0 eV, it can response to wavelength up to 620 nm. It exhibits much higher photocatalytic inactivation efficiency than some of the well investigated VLD photocatalysts, such as CdS and Bi<sub>2</sub>O<sub>3</sub>, etc. [29]. Inspired by the merits of heterojunction and based on the band alignment between g-C<sub>3</sub>N<sub>4</sub> and m-Bi<sub>2</sub>O<sub>4</sub>, it is reasonable to design an all-solid state heterojunction structured g-C<sub>3</sub>N<sub>4</sub>/m-Bi<sub>2</sub>O<sub>4</sub>.

In this study, m-Bi<sub>2</sub>O<sub>4</sub> can be modified onto g-C<sub>3</sub>N<sub>4</sub> nanosheets by a one-pot hydrothermal method using NaBiO<sub>3</sub> as Bi precursor. Hence, if the g-C<sub>3</sub>N<sub>4</sub>/m-Bi<sub>2</sub>O<sub>4</sub> photocatalyst follows the Z-scheme mechanism, the composite might also be an efficient photocatalyst for *E. coli* inactivation. However, to the best of our knowledge, no corresponding research has been reported, which made us focus on the actual mechanism of the g-C<sub>3</sub>N<sub>4</sub>/m-Bi<sub>2</sub>O<sub>4</sub> photocatalyst. Therefore, the structure and charge transfer process of the g-C<sub>3</sub>N<sub>4</sub>/m-Bi<sub>2</sub>O<sub>4</sub> heterojunction were characterized by various methods. The bacterial inactivation mechanism of the g-C<sub>3</sub>N<sub>4</sub>/m-Bi<sub>2</sub>O<sub>4</sub> heterojunction structure was also deeply explored. The morphological change of *E. coli* K-12 during the photocatalytic process was also investigated to evaluate the potential of the hybrid photocatalyst to enhance bacterial inactivation.

## 2. Experimental section

### 2.1. Preparation of photocatalysts

All chemicals were purchased in analytical grade and used without further purification. To synthesize g-C<sub>3</sub>N<sub>4</sub>, a given amount of melamine was placed in a covered crucible and heated to 520 °C at a heating rate of 20 °C/min and kept at 520 °C for 4 h [30]. To synthesize m-Bi<sub>2</sub>O<sub>4</sub>, a suitable amount of NaBiO<sub>3</sub> powder was dispersed in water and put into a 100 mL Teflon lined stainless autoclave, then heated in an oven at 160 °C for 8 h [27]. In order to modify the sur-

face of g-C<sub>3</sub>N<sub>4</sub> with m-Bi<sub>2</sub>O<sub>4</sub>, different amount of NaBiO<sub>3</sub> was added to react with g-C<sub>3</sub>N<sub>4</sub> via the hydrothermal reaction at 160 °C for 8 h. The resulting mixture was centrifuged and washed for several times with deionized water (18.2 MΩ·cm). Finally, the as-obtained precipitate was dried in a vacuum drier for 24 h. The BiOBr and N-TiO<sub>2</sub> were prepared following the methods in References [31] and [32].

### 2.2. Sample characterization

UV-vis diffuse-reflectance spectra (UV-vis DRS) of the as-prepared photocatalysts were recorded on a Solid Spec-3700 DUV spectrophotometer using BaSO<sub>4</sub> as reference and were converted from reflection to absorption by the Kubelka-Munk method. The powder X-ray diffraction (XRD) patterns were recorded on a Bruker D8 diffractometer with monochromated Cu Kα radiation (λ = 1.5418 Å). Fluorescence spectra were monitored with a fluorescence spectrophotometer (Hitachi, Model F-7000) equipped with a PC recorder. Surface electronic states were analyzed by an X-ray photoelectron spectrometer (XPS, ESCALAB MK II). The morphology of the product was characterized by a scanning electron microscopy with energy dispersive X-ray spectroscopy (FESEM-EDX, FEI, Quanta 400 FEG) and a transmission electron microscope (TEM, JEOL JSM-6700F).

### 2.3. Photocatalytic bacterial inactivation

*E. coli* K-12 was chosen as the model bacterium to evaluate the photocatalytic inactivation efficiency of the prepared photocatalysts. Bacterial cells were firstly cultured in nutrient broth at 37 °C for 16 h with shaking, and then harvested by centrifugation at 10,000 rpm for 1 min. The bacterial pellets were then washed with sterilized saline (0.9% NaCl) solution two times in a centrifuge and re-suspended in a sterilized saline solution to obtain suitable concentration of *E. coli*. Then, 20 mg of the prepared photocatalyst was added into 50 mL solution containing 6 log<sub>10</sub> cfu/mL of bacterial suspension. The reaction solution was stirred with a magnetic stirrer throughout the experiment. A Xenon lamp (300 W) with a UV cut-off filter (λ < 400 nm) was used as the light source with light intensity fixed at 193 mW/cm<sup>2</sup> (light emission spectrum is shown in Fig. S1). Then, at different time intervals, aliquot samples were collected and uniformly spread on nutrient agar plates after serial dilutions using the sterilized saline solution. The plates were incubated at 37 °C for 24 h to determine the viable cell count. All the inactivation experiments were conducted in triplicate.

### 2.4. Photoelectrochemical experiments

As-prepared photocatalysts were dispersed in α-naphthol (0.5 wt%) solution and ground for 10 min. The resultant slurry was then blade coated on a 1 × 1 cm<sup>2</sup> fluorine tin oxide (FTO) glass substrate with a glass slide, then the film was dried in air. Photoelectrochemical experiments were performed in a conventional three-electrode cell with a platinum plate (1 × 1 cm<sup>2</sup>) as the counter electrode and a saturated calomel electrode (SCE) as the reference electrode on an electrochemical workstation (CHI660C, Chenhua, China). The prepared working electrode was positioned in the middle of a 0.1 M Na<sub>2</sub>SO<sub>4</sub> aqueous solution with the glass side facing to the incident light.

### 2.5. Reactive species analysis

Nitro blue tetrazolium (NBT) at 0.025 mM was used to detect the production of <sup>•</sup>O<sub>2</sub><sup>-</sup> through measuring the absorbance by a UV-vis spectrophotometer at 259 nm [33]. Terephthalic acid (TA) at 0.5 mM in NaOH (2 mM) solution was used to detect the formation

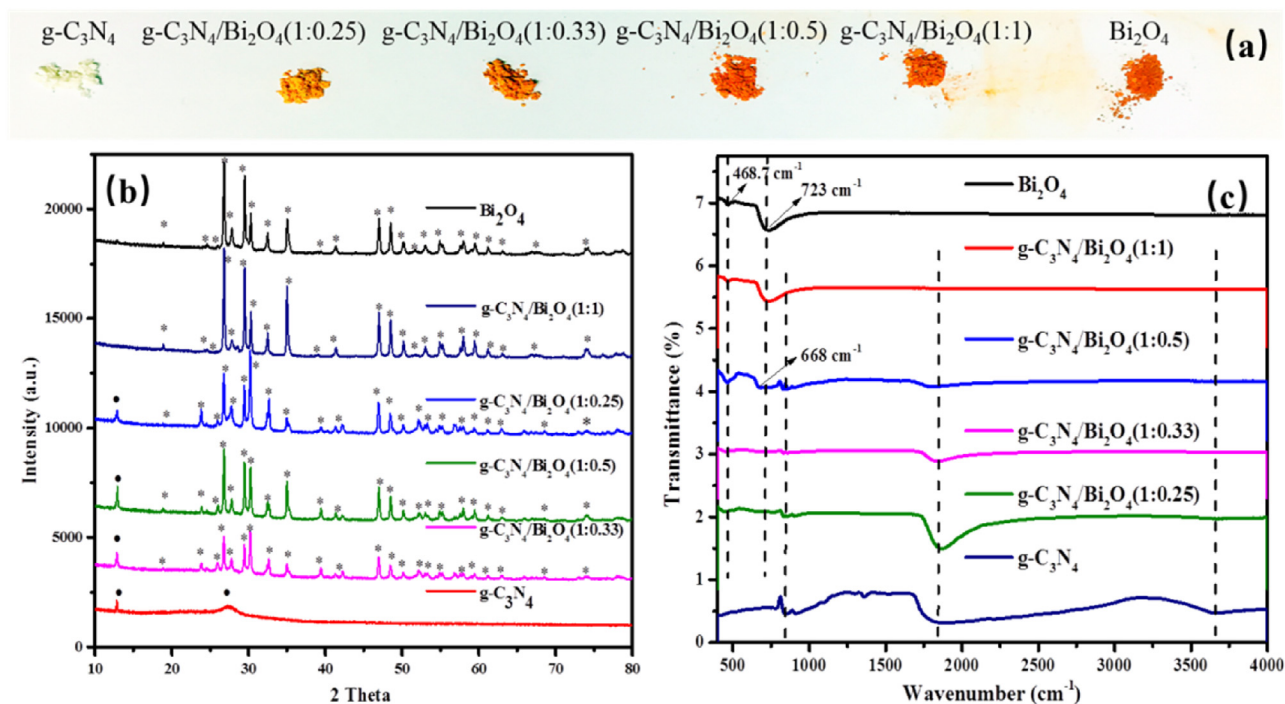


**Fig. 1.** (a) Photos of  $g\text{-C}_3\text{N}_4$ ,  $g\text{-C}_3\text{N}_4/m\text{-Bi}_2\text{O}_4$  and  $m\text{-Bi}_2\text{O}_4$  powders showing the different colors, (b) XRD patterns and (c) FTIR spectrum of  $g\text{-C}_3\text{N}_4$ ,  $g\text{-C}_3\text{N}_4/m\text{-Bi}_2\text{O}_4$  and  $m\text{-Bi}_2\text{O}_4$ .

of  $\cdot\text{OH}$  through measuring the spectrum on a fluorescence spectrophotometer at an excitation wavelength of 365 nm.  $\text{H}_2\text{O}_2$  was analyzed based on the reaction of  $\text{H}_2\text{O}_2$  with coumarin to form a high fluorescent compound named 7-hydroxycoumarin, and was then measured on a fluorescence spectrophotometer with emission at 456 nm [33]. Electron paramagnetic resonance (EPR) spectra of  $\cdot\text{OH}$  and  $\cdot\text{O}_2^-$  were recorded on a Bruker ElexsysE500 spectrometer by applying an X-band (9.43 GHz, 1.5 mW) microwave with sweeping magnetic field at 110 K in cells that can be connected to a conventional high-vacuum apparatus (residual pressure  $< 10^{-4}$  mbar).

## 2.6. Fourier transform infrared (FT-IR) spectroscopy

Samples were prepared by the following procedure: the suspensions at different reaction times were evaporated by a freeze-drying method, then the dry residue was supported on KBr pellets for FTIR measurement. A FTS-4000 Varian Excalibur Series FTIR spectrometer with attenuated total reflection (ATR) (Varian, USA) was used to collect the infrared spectra. Spectra from 4000 to  $800\text{ cm}^{-1}$  were collected with a resolution of  $4\text{ cm}^{-1}$ , and the ordinate was expressed as absorbance. Each spectrum was an average of 256 scans with automatic baseline correction.

## 3. Results and discussion

### 3.1. Structural and optical characterizations of $g\text{-C}_3\text{N}_4/m\text{-Bi}_2\text{O}_4$ hybrid photocatalyst

After the synthesis of pure  $g\text{-C}_3\text{N}_4$ ,  $m\text{-Bi}_2\text{O}_4$  and  $g\text{-C}_3\text{N}_4/m\text{-Bi}_2\text{O}_4$ , it is obvious to find that the modification with increasing  $m\text{-Bi}_2\text{O}_4$  content changes the color of  $g\text{-C}_3\text{N}_4$  from light yellow to red (Fig. 1a), implying increased absorption in visible light. As shown in the XRD patterns (Fig. 1b),  $g\text{-C}_3\text{N}_4$  sample shows its characterization peaks at  $27.4^\circ$  and  $13.0^\circ$ , which can be indexed to the (002) and (100) diffraction plane of the graphite-like carbon nitride

(JCPDS-501250) [16]. Pure  $m\text{-Bi}_2\text{O}_4$  exhibits identical diffraction peaks to the monoclinic phase of  $m\text{-Bi}_2\text{O}_4$  (JCPDS-830410) [21]. The main characteristic diffraction peaks of  $g\text{-C}_3\text{N}_4/m\text{-Bi}_2\text{O}_4$  hybrid materials did not change significantly after  $m\text{-Bi}_2\text{O}_4$  hybridized with  $g\text{-C}_3\text{N}_4$ , confirming the co-existence of  $g\text{-C}_3\text{N}_4$  and  $m\text{-Bi}_2\text{O}_4$  in the  $g\text{-C}_3\text{N}_4/m\text{-Bi}_2\text{O}_4$  hybrid materials. With the increase of  $m\text{-Bi}_2\text{O}_4$  concentration, the intensity of diffraction peaks of  $m\text{-Bi}_2\text{O}_4$  increase gradually at the expense of  $g\text{-C}_3\text{N}_4$  peaks, reflecting their contents in the  $g\text{-C}_3\text{N}_4/m\text{-Bi}_2\text{O}_4$  hybrids. Moreover, the XRD patterns of all the composites are well corresponding to  $\text{Bi}_2\text{O}_4$  or  $g\text{-C}_3\text{N}_4$ , respectively, indicating there are no impurities formed in the composites.

The FT-IR spectra of  $g\text{-C}_3\text{N}_4$ ,  $m\text{-Bi}_2\text{O}_4$ , and  $g\text{-C}_3\text{N}_4/m\text{-Bi}_2\text{O}_4$  samples are shown in Fig. 1c. Pure  $g\text{-C}_3\text{N}_4$  exhibits several strong characteristic peaks in the range of  $1600\text{--}2000\text{ cm}^{-1}$ , which can be ascribed to the typical stretching vibration of C–N heterocycles. The broad peaks at  $3500\text{--}3700\text{ cm}^{-1}$  can be assigned to the stretching vibration mode of H–N and C–H [34]. In addition, the sharp peak at  $810\text{ cm}^{-1}$  is the breathing mode of triazine units [34]. For pure  $m\text{-Bi}_2\text{O}_4$ ,  $468.7$  and  $723\text{ cm}^{-1}$  is assigned as the symmetric stretching vibration peak of the Bi–O band in the  $m\text{-Bi}_2\text{O}_4$  structure [16]. Especially, the FT-IR spectra of  $g\text{-C}_3\text{N}_4/m\text{-Bi}_2\text{O}_4$  composites exhibit an overlap of both  $g\text{-C}_3\text{N}_4$  and  $m\text{-Bi}_2\text{O}_4$ . The intensity of the peak at  $468.7$  and  $723\text{ cm}^{-1}$  increases with an increase of  $m\text{-Bi}_2\text{O}_4$  content, and a little shift (about  $5\text{ cm}^{-1}$ ) of the two IR peaks in the  $g\text{-C}_3\text{N}_4/m\text{-Bi}_2\text{O}_4$  hybrids can be observed. The shifts of these functional groups indicate the chemical interaction and formation of cross-linked connections and covalent bonds, strengthening their chemical interaction between  $g\text{-C}_3\text{N}_4$  and  $m\text{-Bi}_2\text{O}_4$ .

Fig. 2a–f show the SEM images of the as-prepared photocatalysts. Pure  $g\text{-C}_3\text{N}_4$  polymer is an aggregation of many wrinkled sheets with irregular shapes (Fig. 2a), while  $m\text{-Bi}_2\text{O}_4$  exhibits as nanorods with a diameter of ca.  $2\text{--}5\text{ }\mu\text{m}$  (Fig. 2f). As for  $g\text{-C}_3\text{N}_4/m\text{-Bi}_2\text{O}_4$  composites, a few  $m\text{-Bi}_2\text{O}_4$  nanorods are coated on the surface of  $g\text{-C}_3\text{N}_4$ , likely due to the rolling of lamellar  $g\text{-C}_3\text{N}_4$  driven by the surface tension. Moreover, the EDX patterns (Fig. 2g) con-

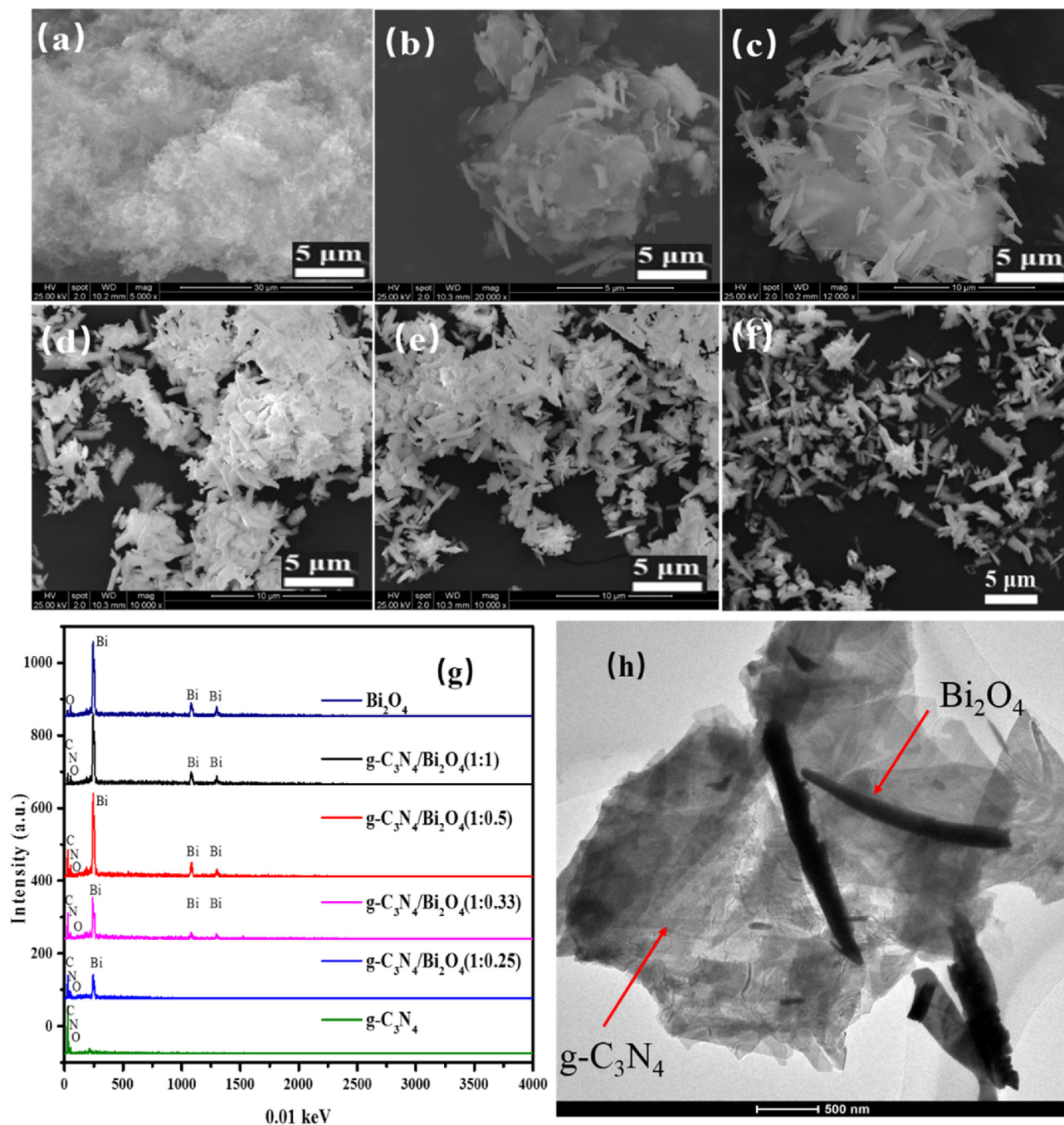


**Fig. 2.** SEM images of pure  $g\text{-C}_3\text{N}_4$  (a),  $g\text{-C}_3\text{N}_4/\text{m-Bi}_2\text{O}_4(1:0.25)$  (b),  $g\text{-C}_3\text{N}_4/\text{m-Bi}_2\text{O}_4(1:0.33)$  (c),  $g\text{-C}_3\text{N}_4/\text{m-Bi}_2\text{O}_4(1:0.5)$  (d),  $g\text{-C}_3\text{N}_4/\text{m-Bi}_2\text{O}_4(1:1)$  (e), and pure  $\text{m-Bi}_2\text{O}_4$  (f), EDX spectra (g), and TEM images (h) of  $g\text{-C}_3\text{N}_4$ ,  $g\text{-C}_3\text{N}_4/\text{m-Bi}_2\text{O}_4(1:0.5)$  and  $\text{m-Bi}_2\text{O}_4$ .

firm that the  $g\text{-C}_3\text{N}_4/\text{m-Bi}_2\text{O}_4$  composites not only contain C, N, and O, but also Bi elements, in which Bi contents were increased with an increase of  $\text{m-Bi}_2\text{O}_4$  contents. TEM images further verify that the sample consists of micron-sized  $\text{m-Bi}_2\text{O}_4$  rods wrapped with lamellar texture of  $g\text{-C}_3\text{N}_4$  (Figs. 2 h and S2).

XPS was further employed to investigate the surface chemical composition and chemical states of the  $g\text{-C}_3\text{N}_4$ ,  $\text{m-Bi}_2\text{O}_4$  and  $g\text{-C}_3\text{N}_4/\text{m-Bi}_2\text{O}_4$  samples, wherein carbon, nitrogen, bismuth and oxygen species were detected (Fig. 3a). Fig. 3b shows the two peaks at 284.6 and 288.1 eV of C1 s spectra, which can be respectively attributed to the C and the N=C=N coordination in pure  $g\text{-C}_3\text{N}_4$  and  $g\text{-C}_3\text{N}_4/\text{m-Bi}_2\text{O}_4$  [35]. Especially, the intensity of C 1 s peaks at 284.6 eV in  $g\text{-C}_3\text{N}_4/\text{m-Bi}_2\text{O}_4$  was higher than that of pure  $g\text{-C}_3\text{N}_4$ ,

indicating the  $\text{m-Bi}_2\text{O}_4$  hybridized with  $g\text{-C}_3\text{N}_4$  could result in inner shift of C 1 s orbit. The N1 s spectra of  $g\text{-C}_3\text{N}_4$  and  $g\text{-C}_3\text{N}_4/\text{m-Bi}_2\text{O}_4$  in Fig. 3c can be deconvoluted into three peaks, which are ascribed to  $\text{sp}^2$  hybridized aromatic N bonded to carbon atom (C=N-C, 398.5 eV), tertiary N bonded to carbon atom (C-(N)3, 399.8 eV) and quaternary N bonded three carbon atoms (N-(C)3, 401.3 eV) in the aromatic cycles, respectively [36]. Especially, there is a weakest peak at 404.3 eV ( $\pi$ -excitations) of N only observed in pure  $g\text{-C}_3\text{N}_4$  rather than  $g\text{-C}_3\text{N}_4/\text{m-Bi}_2\text{O}_4$ . It implies that  $\text{m-Bi}_2\text{O}_4$  covered up the  $\pi$ -excitations and coupled with  $g\text{-C}_3\text{N}_4$  via an interaction using  $\pi$ -electrons of CN heterocycles, rather than coupled with sole C or N atoms of  $g\text{-C}_3\text{N}_4$  [37]. The O1 s spectra of  $g\text{-C}_3\text{N}_4/\text{m-Bi}_2\text{O}_4$  and  $\text{m-Bi}_2\text{O}_4$  were shown in Fig. 3d. For

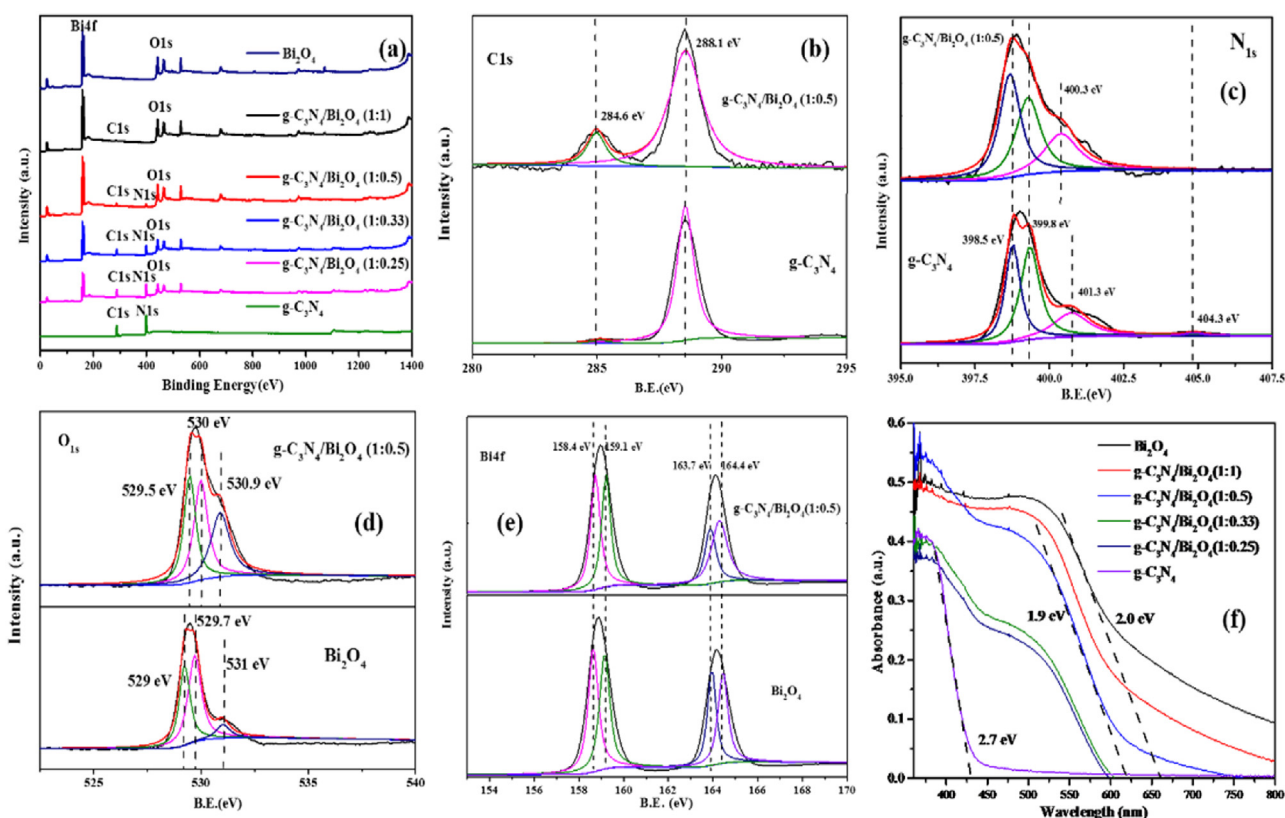


**Fig. 3.** (a) XPS spectra of  $m\text{-Bi}_2\text{O}_4$ ,  $g\text{-C}_3\text{N}_4/m\text{-Bi}_2\text{O}_4$  and  $g\text{-C}_3\text{N}_4$ , High-resolution XPS spectra of (b) C 1s, (c) N 1s, (d) O 1s, and (e) Bi 4f of  $m\text{-Bi}_2\text{O}_4$ ,  $g\text{-C}_3\text{N}_4/m\text{-Bi}_2\text{O}_4$  (1:0.5) and  $g\text{-C}_3\text{N}_4$ . (f) UV-vis absorption spectra of  $g\text{-C}_3\text{N}_4$ ,  $g\text{-C}_3\text{N}_4/m\text{-Bi}_2\text{O}_4$  (1:0.5) and  $m\text{-Bi}_2\text{O}_4$ .

pure  $m\text{-Bi}_2\text{O}_4$ , 529.9 and 531.0 eV was attributed to crystal lattice O atoms (Bi-O) and surface OH, respectively [16,27]. The coupling of  $g\text{-C}_3\text{N}_4$  and  $m\text{-Bi}_2\text{O}_4$  resulted in a higher binding energy of crystal lattice O at 529.9 eV, indicating the coupling happened at O atoms for  $m\text{-Bi}_2\text{O}_4$ . Actually,  $m\text{-Bi}_2\text{O}_4$  mainly contains terminal O atoms in its crystal structure. It indicates that the  $m\text{-Bi}_2\text{O}_4$  is coupled to  $g\text{-C}_3\text{N}_4$  via O-bridging. Fig. 3e displays the Bi 4f spectra of  $m\text{-Bi}_2\text{O}_4$  and  $g\text{-C}_3\text{N}_4/m\text{-Bi}_2\text{O}_4$ , the strong peaks of Bi 4f<sub>7/2</sub> (or 4f<sub>5/2</sub>) can be deconvoluted well into two bimodal peaks at binding energy of 158.4 and 159.1 eV (or at 163.7 and 164.4 eV), which represent Bi(III) and Bi(V) of  $m\text{-Bi}_2\text{O}_4$  [16,27]. Especially, the binding energies of the Bi peaks in  $g\text{-C}_3\text{N}_4/m\text{-Bi}_2\text{O}_4$  are a little higher than pure  $m\text{-Bi}_2\text{O}_4$ , such results could be similarly attributed to the interaction of  $g\text{-C}_3\text{N}_4$  with  $m\text{-Bi}_2\text{O}_4$ , resulting in inner shift of Bi 4f orbits. All the observed shifts for binding energy in the XPS spectra can be attributed to the intense interaction of  $g\text{-C}_3\text{N}_4$  and  $m\text{-Bi}_2\text{O}_4$ , further confirming the successful formation of the heterojunctions.

Fig. 3f shows the UV-vis DRS of  $g\text{-C}_3\text{N}_4$ ,  $m\text{-Bi}_2\text{O}_4$ , and  $g\text{-C}_3\text{N}_4/m\text{-Bi}_2\text{O}_4$ . Modification of  $m\text{-Bi}_2\text{O}_4$  extended the absorption edge of  $g\text{-C}_3\text{N}_4$  in the visible light region, as evidenced by the emerging absorption bands red-shifts regularly from 430 nm to 655 nm with increasing of  $m\text{-Bi}_2\text{O}_4$  content. The increased visible light absorption for  $g\text{-C}_3\text{N}_4/m\text{-Bi}_2\text{O}_4$  suggests that the intermolecular interaction occurs between  $g\text{-C}_3\text{N}_4$  and  $m\text{-Bi}_2\text{O}_4$ , thereby a narrowed bandgap obtained in hybrid  $g\text{-C}_3\text{N}_4/m\text{-Bi}_2\text{O}_4$ . The estimated bandgaps for pure  $\text{Bi}_2\text{O}_3$  (2.0 eV) and  $g\text{-C}_3\text{N}_4$  (2.7 eV) agree well with the reported references [27,38], whereas the calculated band gap of  $g\text{-C}_3\text{N}_4/m\text{-Bi}_2\text{O}_4$  (1:0.5) is 2.3 eV. In conclusion, all the characterization results of  $g\text{-C}_3\text{N}_4/\text{Bi}_2\text{O}_3$  hybrid nanocomposites suggest the effective assembly of  $m\text{-Bi}_2\text{O}_4$  nanorods on  $g\text{-C}_3\text{N}_4$  nanosheets, as well as the successful synthesis of  $g\text{-C}_3\text{N}_4/m\text{-Bi}_2\text{O}_4$  nanocomposites.

### 3.2. Photocatalytic inactivation of *E. coli*

The *E. coli* inactivation performance was used to evaluate the visible light driven photocatalytic activity of as-prepared photocatalysts. As Fig. 4a shows, within 2-h light irradiation, a 4- $\log_{10}$  cfu/mL reduction in *E. coli* population in the presence of pure  $m\text{-Bi}_2\text{O}_4$  was achieved, and an approximately 1.5- $\log_{10}$  cfu/mL reduction of *E. coli* was obtained when pure  $g\text{-C}_3\text{N}_4$  was present. Fortunately, all  $g\text{-C}_3\text{N}_4/\text{Bi}_2\text{O}_3$  samples demonstrate an enhanced photocatalytic inactivation activity than both pure photocatalysts. With the increase of  $m\text{-Bi}_2\text{O}_4$  contents in  $g\text{-C}_3\text{N}_4/m\text{-Bi}_2\text{O}_4$  from 1:0.25 to 1:0.5, an improvement of *E. coli* inactivation efficiency was obtained, which may be explained by the increased formation of heterojunctions between  $g\text{-C}_3\text{N}_4$  and  $\text{Bi}_2\text{O}_3$  in the composites. The highest photocatalytic inactivation activity was achieved with the  $g\text{-C}_3\text{N}_4/\text{Bi}_2\text{O}_3$  (1:0.5), which could completely inactivate 6- $\log_{10}$  cfu/mL *E. coli* within 1.5 h. As shown in Fig. S3, the performance was superior to the well documented BiOBr (2.5 h) and comparable to that of N-TiO<sub>2</sub>, as the time for total inactivation of 6- $\log E. coli$  by BiOBr and N-TiO<sub>2</sub> were 2.5 h and 1.5 h, respectively. However, further increasing the ratio of  $g\text{-C}_3\text{N}_4/m\text{-Bi}_2\text{O}_4$  to 1:1, a decreased photocatalytic inactivation performance was observed (1.75 h was needed for total inactivation of 6- $\log_{10}$  cfu/mL *E. coli*). When the  $m\text{-Bi}_2\text{O}_4$  contents were too high, the efficient heterojunction interface did not increase distinctly, whereas the excessive  $m\text{-Bi}_2\text{O}_4$  with narrow band gap would act as the recombination center of photo-generated electrons and holes. Thus, the drop of the productivity should be ascribed to the decreasing the separation efficiency of electron-hole pairs. To further investigate the effect of the  $g\text{-C}_3\text{N}_4$  modification and confirm the above-proposed mechanisms, the photoluminescence (PL) spectra of  $g\text{-C}_3\text{N}_4/m\text{-Bi}_2\text{O}_4$  were obtained. PL spectra reveal the migration, transfer, and recombination pro-

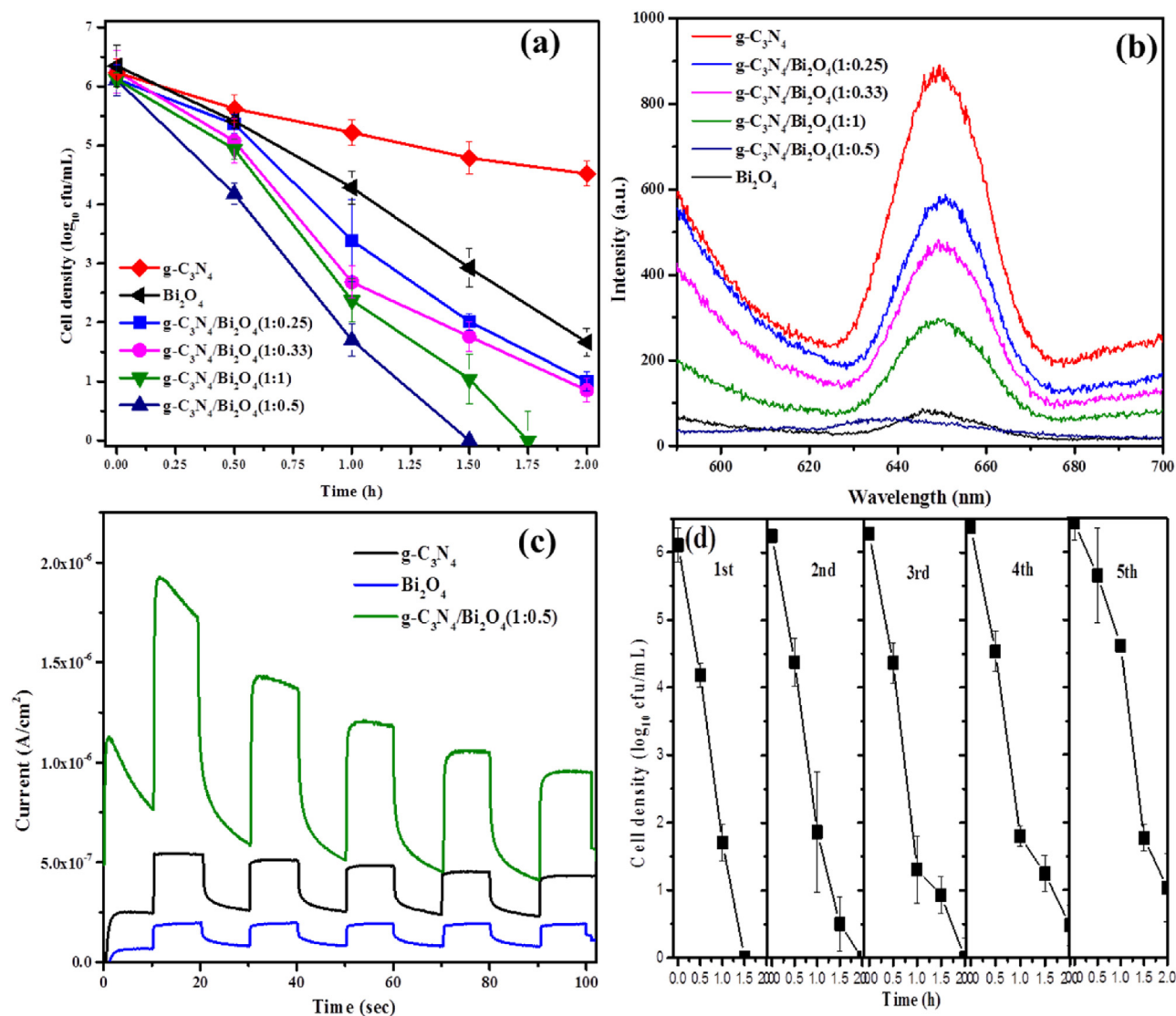


**Fig. 4.** (a) Photocatalytic inactivation of *E. coli* K-12 by  $m\text{-Bi}_2\text{O}_4$ ,  $g\text{-C}_3\text{N}_4/m\text{-Bi}_2\text{O}_4$  and  $g\text{-C}_3\text{N}_4$ ; (b) Photoluminescence spectra of  $m\text{-Bi}_2\text{O}_4$ ,  $g\text{-C}_3\text{N}_4/m\text{-Bi}_2\text{O}_4$  and  $g\text{-C}_3\text{N}_4$ ; (c) Photocurrent of  $m\text{-Bi}_2\text{O}_4$ ,  $g\text{-C}_3\text{N}_4/m\text{-Bi}_2\text{O}_4$  (1:0.5) and  $g\text{-C}_3\text{N}_4$ ; (d) Repeated testing of the photocatalytic inactivation of *E. coli* K-12 over  $g\text{-C}_3\text{N}_4/m\text{-Bi}_2\text{O}_4$  (1:0.5). Experimental conditions: [*E. coli* K-12] =  $6 \log_{10}$  cfu/mL, [catalyst] = 0.4 g/L.

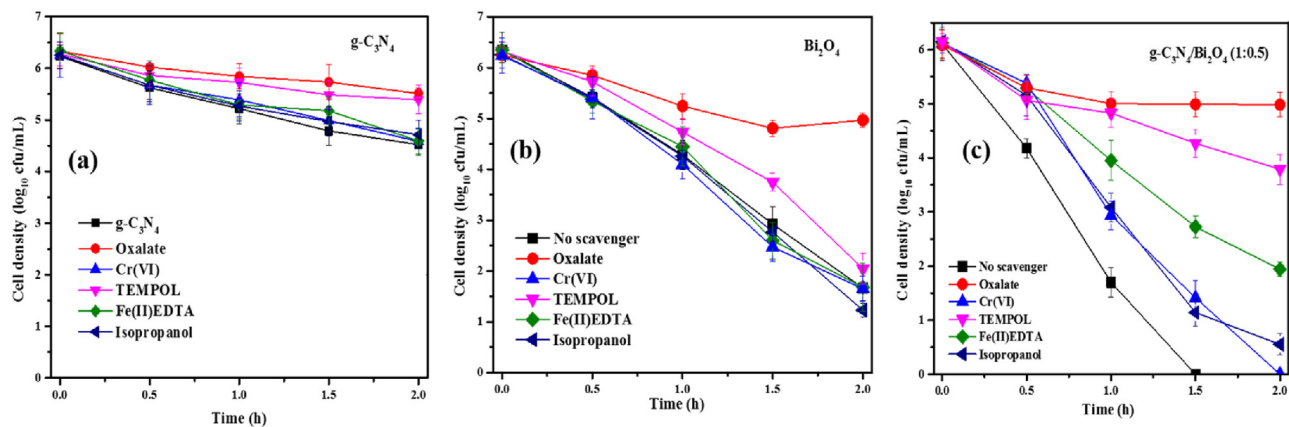


**Fig. 5.** Photocatalytic inactivation of *E. coli* K-12 with different scavengers by (a)  $g\text{-C}_3\text{N}_4$ , (b)  $m\text{-Bi}_2\text{O}_4$ , and (c)  $g\text{-C}_3\text{N}_4/m\text{-Bi}_2\text{O}_4$  (1:0.5) within 2 h visible light irradiation. Experimental conditions: [*E. coli* K-12] =  $6 \log_{10}$  cfu/mL, [catalyst] = 0.4 g/L.

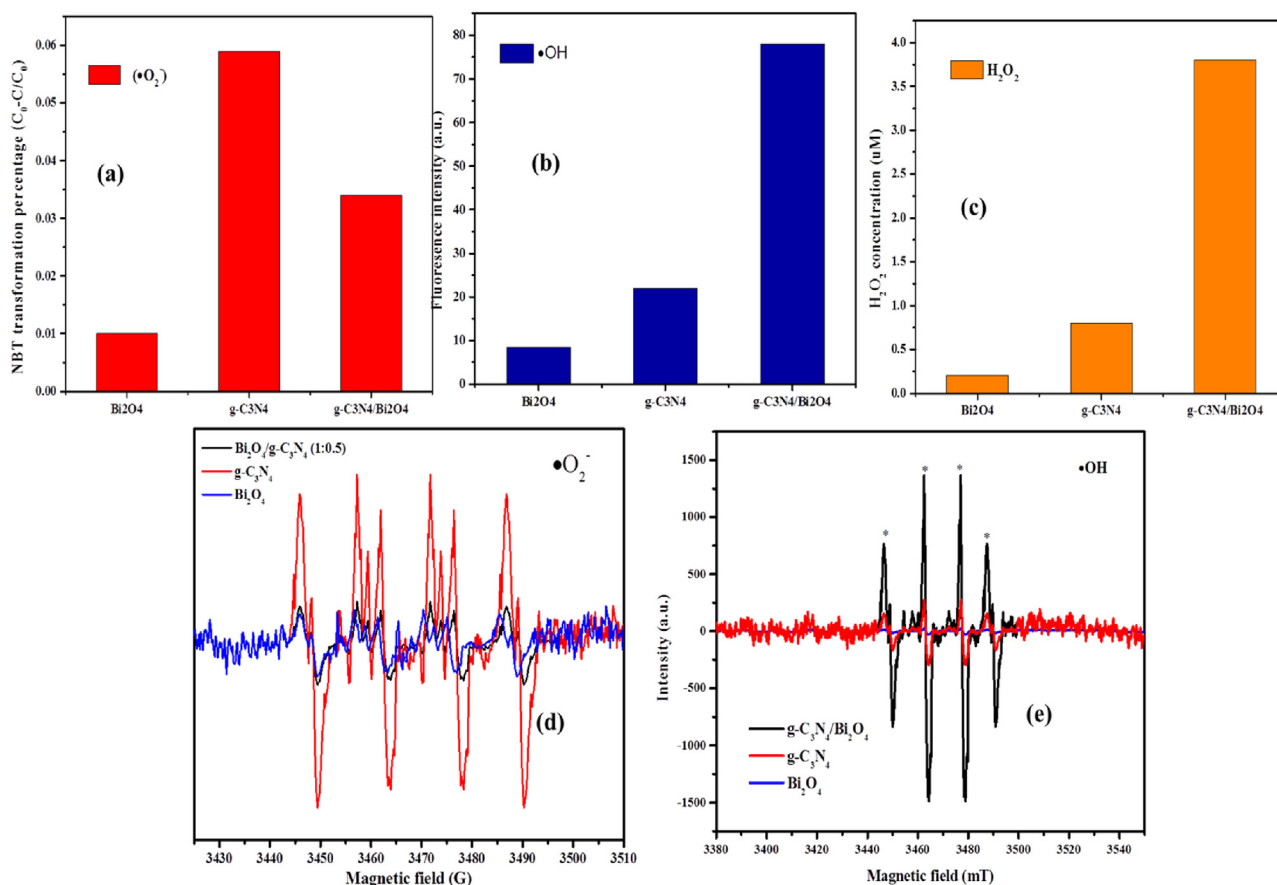


**Fig. 6.** (a) Transformation percentage of NBT concentration (b) Fluorescent intensity of TAOH (c) H<sub>2</sub>O<sub>2</sub> concentration (d) DMPO spin-trapping ESR spectra recorded for •O<sub>2</sub><sup>-</sup> and (e) •OH where the concentration of DMPO was 25 mM when g-C<sub>3</sub>N<sub>4</sub>, m-Bi<sub>2</sub>O<sub>4</sub>, and g-C<sub>3</sub>N<sub>4</sub>/m-Bi<sub>2</sub>O<sub>4</sub>(1:0.5) were irradiated within 2 h visible light irradiation.

cesses of photo-generated electron-hole pairs in semiconductors [39]. Fig. 4b presents the PL spectra of the g-C<sub>3</sub>N<sub>4</sub>/m-Bi<sub>2</sub>O<sub>4</sub> composite photocatalysts at an excitation wavelength of 365 nm. At room temperature, the emission band for pure g-C<sub>3</sub>N<sub>4</sub> was centered at 650 nm, which was attributed to the radiative recombination process of self-trapped excitations. The positions of the g-C<sub>3</sub>N<sub>4</sub>/m-Bi<sub>2</sub>O<sub>4</sub> emission peaks were similar to pure g-C<sub>3</sub>N<sub>4</sub>. However, the emission intensity of the g-C<sub>3</sub>N<sub>4</sub>/m-Bi<sub>2</sub>O<sub>4</sub> composite significantly decreased, with the g-C<sub>3</sub>N<sub>4</sub>/m-Bi<sub>2</sub>O<sub>4</sub> (1:0.5) sample having the weakest intensity. This result clearly indicated that the recombination of photo-generated charge carriers was inhibited in the g-C<sub>3</sub>N<sub>4</sub>/m-Bi<sub>2</sub>O<sub>4</sub> (1:0.5). The same results were obtained using a transient photocurrent responses experiment. As shown in Fig. 4c, although all three samples show a quick response to the light either on or off, the generated transient photocurrent is different. Under light irradiation, the generated photocurrent on the g-C<sub>3</sub>N<sub>4</sub>/m-Bi<sub>2</sub>O<sub>4</sub> (1:0.5) electrode reaches 2 μA, which is four times and eight times higher than g-C<sub>3</sub>N<sub>4</sub> and m-Bi<sub>2</sub>O<sub>4</sub>, respectively. This further demonstrates that g-C<sub>3</sub>N<sub>4</sub>/m-Bi<sub>2</sub>O<sub>4</sub> (1:0.5) is superior to g-C<sub>3</sub>N<sub>4</sub> and m-Bi<sub>2</sub>O<sub>4</sub> in separating electron-hole pairs.

It was reported that photo-corrosion may occur after light irradiation, causing the deactivation of photocatalysts [40]. Therefore, the stability and recyclability of g-C<sub>3</sub>N<sub>4</sub>/m-Bi<sub>2</sub>O<sub>4</sub> (1:0.5) were examined. The results evidenced that the activity of g-C<sub>3</sub>N<sub>4</sub>/m-Bi<sub>2</sub>O<sub>4</sub> (1:0.5) did not decline significantly (5-log<sub>10</sub> cfu/mL of *E. coli* inactivation) after five cycles of *E. coli* inactivation under the visible light irradiation (Fig. 4d). Fortunately, XRD patterns (Fig. S4) also illustrate that the crystal structure of the g-C<sub>3</sub>N<sub>4</sub>/m-Bi<sub>2</sub>O<sub>4</sub> (1:0.5) did not change after the photocatalytic reaction, confirming that

g-C<sub>3</sub>N<sub>4</sub>/m-Bi<sub>2</sub>O<sub>4</sub> (1:0.5) can be evaluated as a stable photocatalyst for bacterial inactivation without photo-corrosion.

### 3.3. Investigation of reactive species

Generally, the photocatalytic bacterial inactivation involves the surface reactions of both photogenerated holes and electrons, which may also produce reactive oxygen species, such as •O<sub>2</sub><sup>-</sup>, •OH and H<sub>2</sub>O<sub>2</sub> to further accelerate the oxidation reactions [41]. The reactive species trapping experiments were employed to investigate the main active species in the photocatalytic *E. coli* inactivation over the g-C<sub>3</sub>N<sub>4</sub>, m-Bi<sub>2</sub>O<sub>4</sub>, and g-C<sub>3</sub>N<sub>4</sub>/m-Bi<sub>2</sub>O<sub>4</sub> (1:0.5), which was useful in deducing the charge transmission route in the hybrid composite photocatalyst [42]. As shown in Fig. 5, with addition of sodium oxalate (a hole scavenger), the *E. coli* inactivation was significantly depressed for g-C<sub>3</sub>N<sub>4</sub>, m-Bi<sub>2</sub>O<sub>4</sub>, and g-C<sub>3</sub>N<sub>4</sub>/m-Bi<sub>2</sub>O<sub>4</sub> (1:0.5), suggesting that the photogenerated holes played a critical role in *E. coli* inactivation in the three cases. On the other hand, when Cr(VI) (an electron scavenger) was added, the *E. coli* inactivation was inhibited over the three photocatalysts, implying that photogenerated electrons were indispensable for directly attack *E. coli* for the three cases.

Considering the fact that conduction band electrons can be captured by O<sub>2</sub> to produce reactive oxygen species, it is essential to explore the role of these species in *E. coli* inactivation. As shown in Fig. 5, addition of TEMPOL (a •O<sub>2</sub><sup>-</sup> scavenger) clearly depressed the *E. coli* inactivation rate on g-C<sub>3</sub>N<sub>4</sub> (Fig. 5a) and g-C<sub>3</sub>N<sub>4</sub>/m-Bi<sub>2</sub>O<sub>4</sub> (1:0.5) (Fig. 5c), but not for m-Bi<sub>2</sub>O<sub>4</sub> (Fig. 5b), implying different roles of •O<sub>2</sub><sup>-</sup> in the three systems. Fig. 5 shows that the addition of Fe(II)-EDTA (a H<sub>2</sub>O<sub>2</sub> scavenger) did not affect the *E. coli* rate over

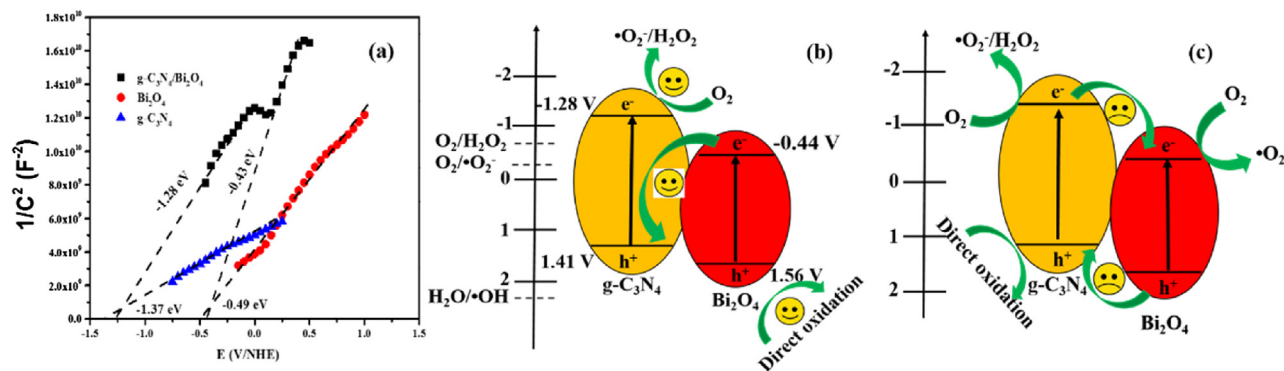
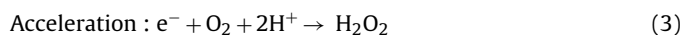
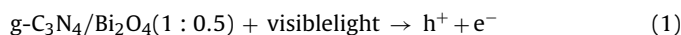


**Fig. 7.** (a) Mott–Schottky plots for g-C<sub>3</sub>N<sub>4</sub>, m-Bi<sub>2</sub>O<sub>4</sub>, g-C<sub>3</sub>N<sub>4</sub>/m-Bi<sub>2</sub>O<sub>4</sub>(1:0.5) at frequency obtained in darkness; Two models of charge separation proposed for g-C<sub>3</sub>N<sub>4</sub>/m-Bi<sub>2</sub>O<sub>4</sub>(1:0.5) under visible irradiation: (b) Conventional donor-acceptor charge transfer, and (c) Z-scheme electron transfer.

g-C<sub>3</sub>N<sub>4</sub> and m-Bi<sub>2</sub>O<sub>4</sub> but g-C<sub>3</sub>N<sub>4</sub>/m-Bi<sub>2</sub>O<sub>4</sub> (1:0.5), indicating that H<sub>2</sub>O<sub>2</sub> involves in the *E. coli* inactivation by g-C<sub>3</sub>N<sub>4</sub>/m-Bi<sub>2</sub>O<sub>4</sub> (1:0.5). Moreover, the addition of isopropanol (a •OH scavenger) slightly inhibited the *E. coli* inactivation rate over g-C<sub>3</sub>N<sub>4</sub>/m-Bi<sub>2</sub>O<sub>4</sub> (1:0.5), whereas no inhibition over g-C<sub>3</sub>N<sub>4</sub> and m-Bi<sub>2</sub>O<sub>4</sub>, suggesting •OH plays a moderate role for g-C<sub>3</sub>N<sub>4</sub>/m-Bi<sub>2</sub>O<sub>4</sub> (1:0.5) rather than g-C<sub>3</sub>N<sub>4</sub> and m-Bi<sub>2</sub>O<sub>4</sub>. On the basis of these comparative observations, it is reasonable to conclude that the photogenerated hole, •O<sub>2</sub><sup>-</sup> and H<sub>2</sub>O<sub>2</sub> are indispensable, playing synergic roles in the *E. coli* inactivation over g-C<sub>3</sub>N<sub>4</sub>/Bi<sub>2</sub>O<sub>4</sub> (1:0.5), whereas that of g-C<sub>3</sub>N<sub>4</sub> are hole and •O<sub>2</sub><sup>-</sup> and m-Bi<sub>2</sub>O<sub>4</sub> are only hole. Obviously, the results indicate the coupling of m-Bi<sub>2</sub>O<sub>4</sub> with g-C<sub>3</sub>N<sub>4</sub> leads to the different photocatalytic mechanism.

To further analyze the roles of different reactive oxygen species in pure g-C<sub>3</sub>N<sub>4</sub>, pure m-Bi<sub>2</sub>O<sub>4</sub> and g-C<sub>3</sub>N<sub>4</sub>/m-Bi<sub>2</sub>O<sub>4</sub> (1:0.5), the detailed •O<sub>2</sub><sup>-</sup>, •OH and H<sub>2</sub>O<sub>2</sub> semi-quantification experiments were used. Fig. 6a–c shows the transformation percentage of NBT (quantification experiments of •O<sub>2</sub><sup>-</sup> production), the fluorescent intensity of TAOH (quantification experiments of •OH production), the concentration of H<sub>2</sub>O<sub>2</sub> within 2-h visible light irradiation for the three photocatalysts, respectively [43]. For m-Bi<sub>2</sub>O<sub>4</sub>, the transformation percentage of NBT, the fluorescent intensity of TAOH, and the concentration of H<sub>2</sub>O<sub>2</sub> are negligible, indicating there are limited •O<sub>2</sub><sup>-</sup>, •OH and H<sub>2</sub>O<sub>2</sub> formation from the h<sup>+</sup> or e<sup>-</sup> of m-Bi<sub>2</sub>O<sub>4</sub>. The reason is shown as following: the conduction band (CB) potential of m-Bi<sub>2</sub>O<sub>4</sub> (-0.37 eV vs NHE) is similar with the standard potential of E<sub>0</sub>(O<sub>2</sub>/<sup>•</sup>O<sub>2</sub><sup>-</sup>) = -0.33 eV vs NHE), and the standard redox potential of Bi<sup>4+</sup>/Bi<sup>3+</sup> (1.59 eV) is more negative than that of •OH/OH<sup>-</sup> (+1.99 eV), thereby only limited reactive oxygen species can be thermodynamically generated [27]. For g-C<sub>3</sub>N<sub>4</sub>, the CB potential of g-C<sub>3</sub>N<sub>4</sub> (-1.28 eV) is more negative than E<sub>0</sub>(O<sub>2</sub>/<sup>•</sup>O<sub>2</sub><sup>-</sup>) = -0.33 eV vs NHE), thereby g-C<sub>3</sub>N<sub>4</sub> shows obvious transformation percentage of NBT (Fig. 6a), indicating more generation of •O<sub>2</sub><sup>-</sup> for g-C<sub>3</sub>N<sub>4</sub> than m-Bi<sub>2</sub>O<sub>4</sub>. Theoretically, due to the VB potential (+1.57 eV vs NHE) of g-C<sub>3</sub>N<sub>4</sub> is more negative than E<sub>0</sub>(•OH/OH<sup>-</sup>) = +1.99 eV vs NHE), the generation of •OH is thermodynamically forbidden from the h<sup>+</sup> in VB of g-C<sub>3</sub>N<sub>4</sub>. However, the observed fluorescent intensity of TAOH was very high as shown in Fig. 6b, which reveals the •OH production of g-C<sub>3</sub>N<sub>4</sub>, consistent with previous report [44]. In fact, the •OH can also be produced from electrons in CB via a two-electron oxidation pathway (H<sub>2</sub>O<sub>2</sub> → •OH), since in photocatalysis H<sub>2</sub>O<sub>2</sub> can be normally generated through direct reduction (O<sub>2</sub> → H<sub>2</sub>O<sub>2</sub>, -1.18 eV vs NHE) or a multistep reaction (O<sub>2</sub> → •O<sub>2</sub><sup>-</sup> → H<sub>2</sub>O<sub>2</sub>) from oxygen. Fortunately, a 0.75 μM H<sub>2</sub>O<sub>2</sub> was detected in the g-C<sub>3</sub>N<sub>4</sub> system, mainly generated from electron reduction pathway on the CB in Fig. 6c [45].

For the g-C<sub>3</sub>N<sub>4</sub>/m-Bi<sub>2</sub>O<sub>4</sub> (1:0.5) composite, the fluorescent intensity of TAOH and concentration of H<sub>2</sub>O<sub>2</sub> increased to 4 and 5 times, respectively, higher than that of the g-C<sub>3</sub>N<sub>4</sub> system (Fig. 6b, 6c), indicating more photo-generated electrons survived in the CB of g-C<sub>3</sub>N<sub>4</sub>/m-Bi<sub>2</sub>O<sub>4</sub> (1:0.5) and resulted in the increase formation of •OH and H<sub>2</sub>O<sub>2</sub>. However, a decreased transformation percentage of NBT (10.9%) was observed (Fig. 6a), suggesting the electrons in the CB of g-C<sub>3</sub>N<sub>4</sub>/m-Bi<sub>2</sub>O<sub>4</sub> (1:0.5) reacted with O<sub>2</sub> to only produce less •O<sub>2</sub><sup>-</sup> than pure g-C<sub>3</sub>N<sub>4</sub>. This result suggested that H<sub>2</sub>O<sub>2</sub> was likely produced via direct reduction (O<sub>2</sub> → H<sub>2</sub>O<sub>2</sub>) in the g-C<sub>3</sub>N<sub>4</sub>/m-Bi<sub>2</sub>O<sub>4</sub> (1:0.5) suspension, rather than the multistep reaction route (O<sub>2</sub> → •O<sub>2</sub><sup>-</sup> → H<sub>2</sub>O<sub>2</sub>) in g-C<sub>3</sub>N<sub>4</sub>. To further confirm this observation, a DMPO spin-trapping ESR technique was employed to characterize the •O<sub>2</sub><sup>-</sup> species generated during photocatalysis. As shown in Fig. 6d, four characteristic peaks of DMPO•O<sub>2</sub><sup>-</sup> were clearly observed in methanol suspensions of g-C<sub>3</sub>N<sub>4</sub>, whereas only a trace level of DMPO•O<sub>2</sub><sup>-</sup> could be detected for the g-C<sub>3</sub>N<sub>4</sub>/Bi<sub>2</sub>O<sub>4</sub> (1:0.5) under the same conditions. Meanwhile, it was found the intensity of •OH signal was much higher in the composite than pure g-C<sub>3</sub>N<sub>4</sub> and Bi<sub>2</sub>O<sub>4</sub>, further conforming more •OH generated by the composite (Fig. 6e). It is reasonable that more H<sub>2</sub>O<sub>2</sub> generation will dissipate into higher concentration of •OH. Based on the above results, the process of photocatalytic *E. coli* inactivation over g-C<sub>3</sub>N<sub>4</sub>/Bi<sub>2</sub>O<sub>4</sub> (1:0.5) involved Eqs. (1)–(5), in which the step 3 was accelerated.



#### 3.4. Determination of the charge transfer mode

To further reveal the reduction and oxidation reactions occurring at the photocatalyst surface, the band energy alignment of the composites were determined by combining Mott-Schottky plots (Fig. 7a) and UV-vis DRS (Fig. 3f). Both g-C<sub>3</sub>N<sub>4</sub> and m-Bi<sub>2</sub>O<sub>4</sub> samples display n-type semiconductor characteristics. The flat-band potential (equal to CB band in n-type semiconductor) was measured at -1.37 V vs NHE for pure g-C<sub>3</sub>N<sub>4</sub> and -1.28 V vs NHE for the g-C<sub>3</sub>N<sub>4</sub> part in g-C<sub>3</sub>N<sub>4</sub>/Bi<sub>2</sub>O<sub>4</sub>. With the known band gap of 2.69 eV for g-C<sub>3</sub>N<sub>4</sub> (Fig. 3f), the VB potential of g-C<sub>3</sub>N<sub>4</sub> can be calculated to be 1.41 V in the g-C<sub>3</sub>N<sub>4</sub>/Bi<sub>2</sub>O<sub>4</sub> composite. The second linear region in the Mott-Schottky plot of g-C<sub>3</sub>N<sub>4</sub>/m-Bi<sub>2</sub>O<sub>4</sub> is attributed to the CB band of the m-Bi<sub>2</sub>O<sub>4</sub> part, corresponding to a potential of -0.43 V for the m-Bi<sub>2</sub>O<sub>4</sub> part in g-C<sub>3</sub>N<sub>4</sub>/Bi<sub>2</sub>O<sub>4</sub>. Similarly, with the known band gap of 2.0 V for m-Bi<sub>2</sub>O<sub>4</sub> (Fig. 3f), the VB potential of m-Bi<sub>2</sub>O<sub>4</sub>

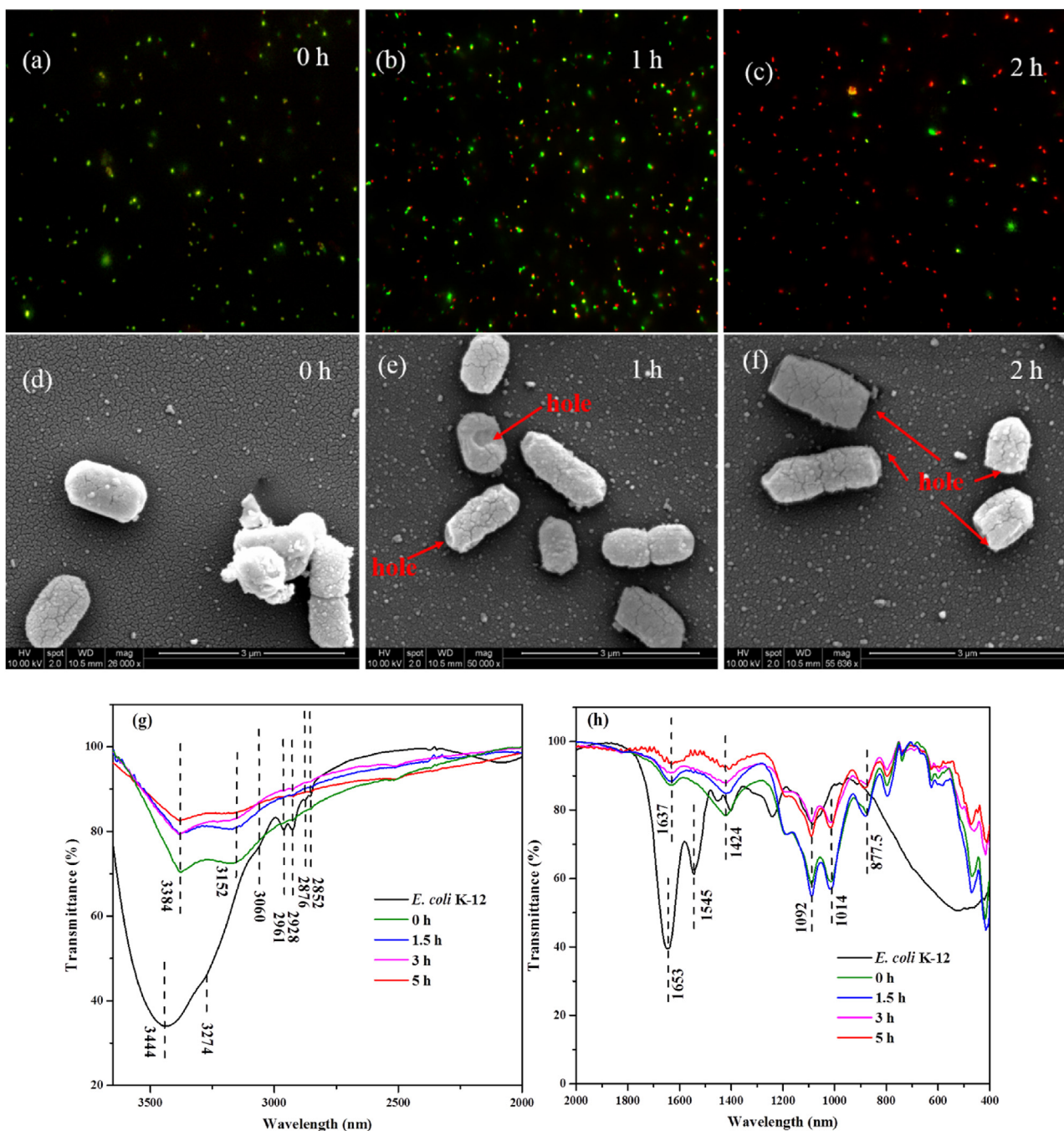


**Fig. 8.** Fluorescence microscopic images (a–c), SEM images (d–f) and FTIR (g–h) spectra of *E. coli* K-12 before and after photocatalytically treated with  $g\text{-C}_3\text{N}_4/m\text{-Bi}_2\text{O}_4$ . Experimental conditions: [*E. coli* K-12] =  $6 \log_{10}$  cfu/mL, [catalyst] = 0.4 g/L.

can be calculated to be 1.57 V in the  $g\text{-C}_3\text{N}_4/m\text{-Bi}_2\text{O}_4$  composite. For pure  $m\text{-Bi}_2\text{O}_4$ , the measured CB band is at  $-0.49$  V and VB band is at 1.51 V, respectively.

The direction of the photogenerated charge across the heterojunctions for the synthesized materials can be inferred by coupling the experimental results with the established band alignment. In the present study,  $m\text{-Bi}_2\text{O}_4$  was deposited on  $g\text{-C}_3\text{N}_4$  surface and the hybrid junctions were formed at the interfacial phases, resulting in inner electrical fields established in the direction from  $g\text{-C}_3\text{N}_4$  to  $m\text{-Bi}_2\text{O}_4$ . When exposing to the visible light, the VB electrons of both  $g\text{-C}_3\text{N}_4$  and  $m\text{-Bi}_2\text{O}_4$  could be excited up. The charge transfer at the interfacial phases may follow the Z-scheme transfer mode (Fig. 7b) or double-transfer mechanism (Fig. 7c). According to above

results in Fig. 6, the electron can enrich on the CB of  $g\text{-C}_3\text{N}_4$  (thereby retaining sufficient capacity to reduce  $\text{O}_2$  species to  $\text{H}_2\text{O}_2$  and  $\bullet\text{OH}$ ), only when the electron and holes in  $g\text{-C}_3\text{N}_4/m\text{-Bi}_2\text{O}_4$  (1:0.5) migrate by the Z-scheme mechanism. Otherwise, if the double-transfer mechanism is adopted, the photogenerated electron would accumulate on the CB of  $m\text{-Bi}_2\text{O}_4$  and result in the dominant reactive species of  $\bullet\text{O}_2^-$  rather than  $\text{H}_2\text{O}_2$ , which is inconsistent with the experimental result.

Under VL irradiation, both  $g\text{-C}_3\text{N}_4$  and  $m\text{-Bi}_2\text{O}_4$  were excited, and the photogenerated holes and electrons were in their VB and CB, respectively. Then, the internal static electric fields of  $m\text{-Bi}_2\text{O}_4$  resulted in that the  $e^-$  of  $m\text{-Bi}_2\text{O}_4$  transfer to the interface between  $g\text{-C}_3\text{N}_4$  and  $m\text{-Bi}_2\text{O}_4$ . The electron located in the CB of  $g\text{-C}_3\text{N}_4$  pos-

essed higher reducing power (by  $-0.84\text{ V}$  in comparison to that of  $\text{m-Bi}_2\text{O}_4$ ), thereby enabling direct reduction of  $\text{O}_2$  to  $\text{H}_2\text{O}_2$  and  $\bullet\text{OH}$  (Eq. (3)), which was consistent with the results presented in Fig. 5 and 6. Meanwhile, the higher level of VB of  $\text{m-Bi}_2\text{O}_4$  (by  $1.71\text{ V}$  in comparison to that of  $\text{g-C}_3\text{N}_4$ ) provided stronger oxidizing power for the hole, thus enabling direct oxidation of *E. coli* (Eq. (5)), which was consistent with the results shown in Fig. 5 and 6. The heterojunction charge separation as illustrated by the Z-scheme reduces the probability of charge recombination that is often encountered in the single-component photocatalyst, thus producing an increased density of holes and electrons for enhanced performance.

### 3.5. Bacterial destruction process

The processed bacterial membrane integrity was visually observed through fluorescence microscopy. As shown in Fig. 8a–c, after staining with a fluorescent dye mixture, the red fluorescent cells increased in number to replace the green fluorescent cells after prolonged treatment, indicating cell membrane rupture during photocatalytic process [46]. Meanwhile, the *E. coli* destruction process using the  $\text{g-C}_3\text{N}_4/\text{m-Bi}_2\text{O}_4$  photocatalyst was also visually observed by SEM. Before treatment, the *E. coli* cell had an intact cell structure and a well preserved rod shape (Fig. 8d). During the inactivation process, the characteristic rod shape of the cell became abnormal, and the cell's shape was distorted with holes (Fig. 8e–f). This point to the fact that sustainably generated RSs can cause a myriad of adverse effects on the cell envelope. Actually, the cell envelope contains essential protein components such as respiratory chain, which generate energy (ATP) with functionalized electron chains, playing a vital role in bacterial metabolism. As Fig. S5a shows, associated with the damaged cell envelope, the cells were almost instantaneously inactivated by metabolic arrest as a consequence of a drastic drop in the ATP level, with ATP level decreased from  $123.8\text{ RLU}/10^3$  to zero after the exposure to VL irradiated  $\text{g-C}_3\text{N}_4/\text{m-Bi}_2\text{O}_4(1:0.5)$  within 1 h. The loss of ATP generation capacity directly caused bacterial death: a lack of ATP limits the cellular energy supply, preventing cellular repair and bacterial growth. Meanwhile, a remarkable decrease in both SOD and CAT activities was observed after 0.5 h and continued thereafter (Fig. S5b–c), further confirming that the defense capacity was overwhelmed by ROS at the initial stage and then decomposed rapidly. Damage to the anti-oxidative defense system will facilitate the ROS flood into cells and aggravate the oxidation of *E. coli*.

FTIR provides a means to identify key functional groups and structures of the cells, and evaluate changes of cells caused through exposure to oxidants [40]. In Fig. 8g, a wide skewed band in the region  $3400\text{--}3600\text{ cm}^{-1}$  due to the  $\text{OH}^-$  vibrations of the absorbed water and  $\text{OH}^-$  on the catalyst surface. For *E. coli* cells alone, the characteristic peaks at  $3274$  and  $3060\text{ cm}^{-1}$  were attributed to amide A and amide B, and the peaks at  $2961$ ,  $2928$ ,  $2876$ , and  $2852\text{ cm}^{-1}$  were assigned to  $\nu_a(\text{CH}_3)$ ,  $\nu_a(\text{CH}_2)$ ,  $\nu_s(\text{CH}_3)$ , and  $\nu_s(\text{CH}_2)$ , respectively. With increasing experimental time to 3 h, the intensity and integral absorbance of these initial *E. coli* spectral profiles quickly shifted, disappeared or decayed. After 5 h, the disappearance of amide A ( $3274\text{ cm}^{-1}$ ) and amide B ( $3060\text{ cm}^{-1}$ ) were observed, and also the peak intensity of the C–H bands ( $2963$ ,  $2927$ ,  $2872$ , and  $2852\text{ cm}^{-1}$ ) were almost undetectable. Concomitantly, the wide band containing  $\text{OH}^-$  vibrations is transformed to a skewed form with a maximum at around  $3384\text{ cm}^{-1}$ . Similarly, Fig. 8h also exhibits significant decay of the  $\text{PO}_2^-$  band near  $1242\text{ cm}^{-1}$  and oligosaccharide bands around  $1014\text{--}1092\text{ cm}^{-1}$ , as well as the amide I band near  $1653\text{ cm}^{-1}$  and the amide II band near  $1545\text{ cm}^{-1}$  after 5 h treatment. Based on above observations, the results revealed that the cell envelope of *E. coli* K-12 were

firstly decomposed, then cytoplasmic components leaked out and degraded, finally resulting in the cell death.

## 4. Conclusions

In summary, an all-solid-state Z-scheme heterojunction ( $\text{g-C}_3\text{N}_4/\text{m-Bi}_2\text{O}_4$ ) has been successfully constructed. As tested for photocatalytic inactivation of *E. coli* under visible light, significant enhancement in photocatalytic activity was observed for  $\text{g-C}_3\text{N}_4/\text{m-Bi}_2\text{O}_4(1:0.5)$  in comparison to the pristine  $\text{g-C}_3\text{N}_4$  and  $\text{m-Bi}_2\text{O}_4$ . The Z-scheme heterojunction creates charge separation with the electron populated to the higher CB and hole to the lower VB, thus enhancing the redox reaction power of the charge carriers. The strong electron of  $\text{g-C}_3\text{N}_4$  can trigger the direct reduction of  $\text{O}_2$  to  $\text{H}_2\text{O}_2$ , collectively work with the strong photogenerated holes of  $\text{m-Bi}_2\text{O}_4$  to attack *E. coli*. This study provides new insights into the rational design of effective photocatalysts that can be operated under visible light, particularly for purifying hospital wastewater contaminated with highly concentrated pathogenic microorganisms.

## Acknowledgement

The project was supported by a research grant (GRF14100115) of the Research Grant Council, Hong Kong SAR Government and the Technology and Business Development Fund (TBF15SCI008) of The Chinese University of Hong Kong to P.K. Wong, and the research grants (21607028, 41603097, 41573086, and 41425015) of National Science Foundation of China to W.J. Wang, D.H. Xia, G.Y. Li, T.C. An, respectively. H.J. Zhao and P.K. Wong were also supported by CAS/SAFEA International Partnership Program for Creative Research Teams of Chinese Academy of Sciences (2015HSC-UE004).

## Appendix A. Supplementary data

Supplementary data associated with this article can be found, in the online version, at <http://dx.doi.org/10.1016/j.apcatb.2017.05.035>.

## References

- [1] D. Haaken, T. Dittmar, V. Schmalz, E. Worch, *Water Res.* 52 (2014) 20–28.
- [2] L.C. Rietveld, D. Norton-Brandao, R. Shang, J. van Agtmaal, J.B. van Lier, *Water Sci. Technol.* 64 (2011) 1540–1546.
- [3] P.H. Dobrowsky, M. De Kwaadsteniet, T.E. Cloete, W. Khan, *Appl. Environ. Microbiol.* 80 (2014) 2307–2316.
- [4] J.A. Soller, M.E. Schoen, A. Varghese, A.M. Ichida, A.B. Boehm, S. Eftim, N.J. Ashbolt, J.E. Ravenscroft, *Water Res.* 66 (2014) 254–264.
- [5] A.C. Eischeid, J.A. Thurston, K.G. Linden, *Crit. Rev. Environ. Sci. Technol.* 41 (2011) 1375–1396.
- [6] E.M. Anastasi, T.D. Wohlsen, H.M. Stratton, M. Katouli, *Water Res.* 47 (2013) 6670–6679.
- [7] AWWA, *Water Treatment: Principles and Practices of Water Supply Operations*, American Water Works Association, Denver, 1995.
- [8] K.M. Parker, T. Zeng, J. Harkness, A. Vengosh, W.A. Mitch, *Environ. Sci. Technol.* 48 (2014) 11161–11169.
- [9] V.K. Sharma, R. Zboril, T.J. McDonald, *J. Environ. Sci. Health B* 49 (2014) 212–228.
- [10] H. Sun, G. Li, X. Nie, H. Shi, P.K. Wong, H.J. Zhao, T. An, *Environ. Sci. Technol.* 48 (2014) 9412–9419.
- [11] L. Xiong, T.W. Ng, Y. Yu, D. Xia, H.Y. Yip, G. Li, T. An, H.J. Zhao, P.K. Wong, *Electrochim. Acta* 153 (2015) 583–593.
- [12] A. Kubacka, M.S. Diez, D. Rojo, R. Bargiela, S. Ciordia, I. Zapico, J.P. Albar, C. Barbas, V. dos Santos, M. Fernandez-Garcia, M. Ferrer, *Sci. Rep.* 4 (2014) 4134.
- [13] C. Ruales-Lonfat, N. Benitez, A. Sienkiewicz, C. Pulgarin, *Appl. Catal. B: Environ.* 160–161 (2014) 286–297.
- [14] C. Santaella, B. Allainmat, F. Simonet, C. Chaneac, J. Labille, M. Auffan, J. Rose, W. Achouak, *Environ. Sci. Technol.* 48 (2014) 5245–5253.
- [15] T. An, J. An, Y. Gao, G. Li, H. Fang, W. Song, *Appl. Catal. B Environ.* 164 (2015) 279–287.
- [16] D. Xia, M.C.I. Lo, *Water Res.* 100 (2016) 393–404.

- [17] X. Yang, C. Cao, L. Erickson, K. Hohn, R. Maghirang, K. Klabunde, J. Catal. 260 (2008) 128–133.
- [18] M. Xing, J. Zhang, F. Chen, Appl. Catal. B: Environ. 89 (2009) 563–569.
- [19] Z. Zhang, J. Long, L. Yang, W. Chen, W. Dai, X. Fu, X. Wang, Chem. Sci. 2 (2011) 1826–1830.
- [20] F. Su, S.C. Mathew, G. Lipner, X.Z. Fu, M. Antonietti, S. Blechert, X. Wang, J. Am. Chem. Soc. 132 (2010) 16299–16301.
- [21] X. Wang, K. Maeda, A. Thomas, K. Takahabe, G. Xin, J.M. Carlsson, K. Domen, M. Antonietti, Nat. Mater. 8 (2009) 76–80.
- [22] Y. Zhang, T. Mori, J. Ye, M. Antonietti, J. Am. Chem. Soc. 132 (2010) 6294–6295.
- [23] J. Zhang, G. Zhang, X. Chen, S. Lin, L. Mohlmann, G. Dolega, G. Lipner, M. Antonietti, S. Blechert, X. Wang, Angew. Chem. Int. Ed. 51 (2012) 3183–3187.
- [24] J. Huang, W.K. Ho, X. Wang, Chem. Commun. 50 (2014) 4338–4340.
- [25] Y. He, L. Zhang, B. Teng, M. Fan, Environ. Sci. Technol. 49 (2015) 649–656.
- [26] L. Ye, J. Liu, Z. Jiang, T. Peng, L. Zan, Appl. Catal. B: Environ. 142–143 (2013) 1–7.
- [27] P. Zhou, J.G. Yu, M. Jaroniec, Adv. Mater. 26 (2014) 4920–4935.
- [28] G. Dong, L. Yang, F. Wang, L. Zang, C. Wang, ACS Catal. 6 (2016) 6511–6519.
- [29] W. Wang, X. Chen, G. Liu, Z. Shen, D. Xia, P.K. Wong, J.C. Yu, Appl. Catal. B: Environ. 176–177 (2015) 444–453.
- [30] Y. He, L. Zhang, B. Teng, M. Fan, Environ. Sci. Technol. 49 (2015) 649–656.
- [31] D. Wu, B. Wang, W. Wang, T. An, G. Li, T.W. Ng, H.Y. Yip, C. Xiong, P.K. Wong, J. Mater. Chem. A 3 (2016) 15148–15155.
- [32] C. Di Valentin, E. Finazzi, G. Pacchioni, A. Selloni, S. Livraghi, M.C. Paganini, E. Giamello, Chem. Phys. 339 (2007) 44–56.
- [33] D. Xia, Z. Shen, G. Huang, W. Wang, J.C. Yu, P.K. Wong, Environ. Sci. Technol. 49 (2015) 6264–6273.
- [34] S. Chen, P. Slattum, C.Y. Wang, L. Zang, Chem. Rev. 115 (2015) 11967–11998.
- [35] Y. Wang, R. Shi, J. Lin, Y. Zhu, Energy Environ. Sci. 4 (2011) 2922–2929.
- [36] L. Qi, J. Yu, M. Jaroniec, Phys. Chem. Chem. Phys. 13 (2011) 8915–8923.
- [37] A. Thomas, A. Fischer, F. Goettmann, M. Antonietti, J.-O. Mueller, R. Schloegl, J.M. Carlsson, J. Mater. Chem. 18 (2008) 4893–4908.
- [38] S. Wang, D. Li, C. Sun, S. Yang, Y. Guan, H. He, Appl. Catal. B: Environ. 144 (2014) 885–892.
- [39] H. Cheng, J. Hou, O. Takeda, X. Guo, H. Zhu, J. Mater. Chem. A 3 (2015) 11006–11013.
- [40] D. Xia, T.W. Ng, T. An, G. Li, Y. Li, H.Y. Yip, H. Zhao, A. Lu, P.K. Wong, Environ. Sci. Technol. 47 (2013) 11166–11173.
- [41] F. Dong, Z. Wang, Y. Li, W.K. Ho, S.C. Lee, Environ. Sci. Technol. 48 (2014) 10345–10353.
- [42] G. Li, X. Nie, J. Chen, Q. Jiang, T. An, P.K. Wong, H. Zhang, H. Zhao, H. Yamashita, Water Res. 86 (2015) 17–24.
- [43] D. Xia, T. An, G. Li, W. Wang, H.J. Zhao, P.K. Wong, Water Res. 99 (2016) 149–161.
- [44] S. Li, G. Dong, R. Hailili, L. Yang, Y. Li, F. Wang, Y. Zeng, C. Wang, Appl. Catal. B: Environ. 190 (2016) 26–35.
- [45] L. Wang, M. Cao, Z. Ai, L. Zhang, Environ. Sci. Technol. 48 (2014) 3354–3362.
- [46] L. Zhang, K.H. Wong, H.Y. Yip, C. Hu, J.C. Yu, C.Y. Chan, P.K. Wong, Environ. Sci. Technol. 44 (2010) 1392–1398.